ACS APPLIED MATERIALS & INTERFACES

Open Access

This article is licensed under CC-BY 4.0

www.acsami.org

Research Article

Perovskite Oxide Interfaces Tailored by Cation Ordering Periodicities: Experimentally Resolved Atomic Structure and Predicted Magnetic Coupling

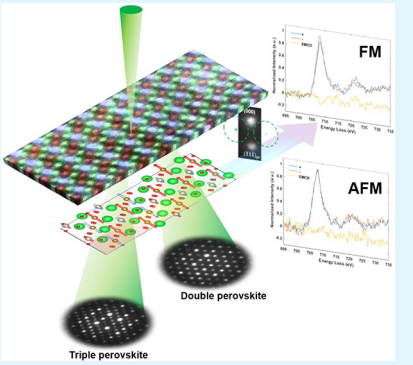
Jie Ren,[‡] Ping-Luen Baron Ho,[*,‡] Lei Jin, Si-Young Choi, Rafal E. Dunin-Borkowski, Joachim Mayer, Sandrine E. M. Heutz, Michele Shelly Conroy, Shik Chi Edman Tsang,[†] and Xiaoyan Zhong[*]

Cite This: *ACS Appl. Mater. Interfaces* 2026, 18, 50054−50063

Read Online

ACCESS | Metrics & More | Article Recommendations | Supporting Information

ABSTRACT: Magnetically coupled interfaces formed from perovskite oxides with different B-site ordering periodicities have not been studied extensively due to challenges in synthesis and a lack of adequate parent phases. Here, we use aberration-corrected analytical scanning transmission electron microscopy to identify the atomic structure and chemistry of a perovskite oxide interface that exhibits different B-site ordering periodicity on the atomic scale. The interface is formed from the 1:1 B-site-ordered double-perovskite $Sr_2Fe_{1+x}Re_{1-x}O_6$ and the 1:2 B-site-ordered triple-perovskite $Sr_3Fe_2ReO_9$. First-principles calculations on the superlattice model with the same modulation of B-site ordering periodicity observed experimentally show that magnetic coupling between Fe and Re atoms at the interface results in characteristics of ferromagnetism, in contrast to the antiferromagnetic nature of the parent phases. The results suggest that tailoring of B-site ordering periodicity for tuning interfacial magnetism at perovskite oxide interfaces can be potentially applied in epitaxial growth of superlattice thin films with magnetically engineered interfaces.



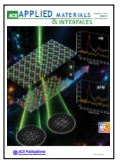
KEYWORDS: *triple- and double-perovskite oxides, interfacial magnetic coupling, electron magnetic circular dichroism, first-principles calculations, scanning transmission electron microscopy*

1. INTRODUCTION

The stacking order of B-site cations plays a significant role in determining the electromagnetic properties of perovskite oxide interfaces,[1,2] allowing researchers to develop a wide range of novel artificial crystals.[3−5] The traditional construction of perovskite oxide interfaces in superlattice thin films typically relies on the use of building blocks that have the same B-cation-ordering periodicity (n:m), resulting in interfaces between $(ABO_3)_n$ and $(AB'O_3)_m$. Previous studies have focused primarily on using the thickness ratios of sub-layers as controllable parameters for modulating B-site cations in thin-film superlattices based on the $-[(ABO_3)_n/(AB'O_3)_m]_k-$ system. Advanced thin-film synthesis methods provide flexible control of the values of n and m in such layers, from a single unit cell up to thicknesses of several nm.[6] The study of superlattices makes interfacial phenomena more evident using repetitions of the same n:m periodicity.[7−11]

In contrast, perovskite oxide interfaces between thin films with different B-site order periodicities, e.g., $-[(ABO_3)_n/(AB'O_3)_m]_k-/-[(ABO_3)_{n'}/(AB'O_3)_{m'}]_{k'}-$, are often overlooked. Generally, such interfaces can be engineered by varying the A-site cations, the B-site cations, the oxygen stoichiometry, or combinations of these variables within the constituent blocks, such as $(A'BO_3)$ and $(A'B'O_3)$. In the present work, the A-site is fixed across the interface, thereby allowing us to focus specifically on the effect of changing the B-site cation ordering periodicity. Compared to conventional perovskites, double-perovskite ($A_2BB'O_6$) and triple-perovskite ($A_3BB'B''O_9$) structures enable a wider range of heterovalent transition-metal combinations at the B-sites. This compositional flexibility provides additional degrees of freedom for tailoring magnetic properties such as half metallicity,[12] giant magnetoresistance (GMR),[13] and multiferroicity.[14] The B-site cation stacking order and periodicity are significantly different between 1:1 B-site-ordered double perovskites and 1:2 B-site-ordered triple perovskites. From the perspective of crystallography, a 1:1 B-site-ordered double perovskite provides crystallographically equivalent 6-fold-coordinated sites B_1 and B_2 with 1:1 layering alternating along $[111]_{pc}$, with an ordering vector of $1/2[111]^*$ in a NaCl-type arrangement.[15] The B_1 and B_2 sites can be occupied either

Received: May 2, 2026
Revised: August 6, 2026
Accepted: August 6, 2026
Published: September 2, 2026



ACS Publications

© 2026 The Authors. Published by American Chemical Society

Downloaded from pubs.acs.org/aamick/article-pdf/18/36/50054/6822221/am-2026-08939f.pdf by guest on 08 November 2026

by elements B and B′ individually or by a combination of B and B′ in certain ratios. In contrast, the 1:2 B-site-ordered triple perovskite contains B_1, B_2, and B_3 atoms on crystallographically triple-equivalent 6-fold-coordinated sites with an ordering vector of 1/3[111]*.

Previous reports have suggested that the cation ratio and periodicity of B and B′ atoms can influence the magnetic susceptibility of double and triple perovskites.[16,17] Among double perovskites, Sr_2FeReO_6 (SFRO) has emerged as a key material due to its high Curie temperature (~400 K), intrinsic ferrimagnetism, and interlayer antiferromagnetic interactions. Structural and compositional modifications of SFRO have further demonstrated its potential to function as a room-temperature ferromagnetic insulator, rendering it a promising candidate for efficient charge transport and spin manipulation under ambient conditions.[16] However, in complex SFRO perovskite oxides, it is essential to distinguish between the thermodynamic stability of the crystallographic host lattice and the kinetic stability of specific ordering or defect states accommodated within that lattice. Our previous studies have demonstrated that, under given temperature and oxygen chemical potential, the double-perovskite framework itself constitutes the stable structural phase, while variations in B-site rock-salt ordering and oxygen nonstoichiometry represent distinct configurational states of the same parent phase rather than separate thermodynamic phases.[18] These ordering or defect states may be readily stabilized during synthesis, particularly under constrained growth conditions, but often evolve irreversibly upon annealing toward a reproducible terminal configuration.[19] Accordingly, subsequent analysis is confined to these thermodynamically stable phases.

The 1:1 B-site-ordered double perovskite can be expressed as $Sr_2Fe_{1+x}Re_{1-x}O_6$ where the x value is used to measure the deviation from ideal 1:1 atomic occupation of Fe and Re in $Sr_2[Fe]_{B_1}[Re]_{B_2}O_6$. For instance, a 1:1 B-site-ordered double-perovskite $Sr_2[Fe]_{B_1}[Re]_{B_2}O_6$ can turn into a semiconductor with spontaneous magnetization below 475 K[20] by changing the element ratio to $Sr_2[Fe]_{B_1}[Fe_{1/3}Re_{2/3}]_{B_2}O_6$ with the x value of 1/3. Fe/Re perovskites with similar nominal compositions may adopt different B-site ordering. Crystallographically, a Fe-rich $Sr_3Fe_2ReO_9$ phase can be described as 1:1 B-site-ordered $Sr_2[Fe_{0.57}Re_{0.43}]_{B_1}[Fe_{0.76}Re_{0.24}]_{B_2}O_6$ with a different Fe to Re ratio on the B_1 and B_2 sites, exhibits ferromagnetic (FM) order below 450 K, and has a saturation magnetization of 1.10 μ_B/mol.[21] Beyond the 1:1 B-site-ordered double-perovskite structure, the $Sr_3Fe_2ReO_9$ phase, which can also be described as 1:2 B-site-ordered $Sr_3[Fe]_{B_1}[Fe]_{B_2}[Re]_{B_3}O_9$ with ordered –[Fe–Fe–Re]$_n$– occupation, is theoretically predicted to be antiferromagnetic (AFM), as identified in our previous research.[22] These examples highlight the fact that periodicity and ordering occupancy have a significant impact on the magnetic behavior of double- and triple-perovskite oxides. The difference in the crystallographic structure between the 1:1 B-site-ordered double-perovskite $Sr_2Fe_{1+x}Re_{1-x}O_6$ and the 1:2 B-site-ordered triple-perovskite $Sr_3Fe_2ReO_9$ therefore makes it possible to construct a perovskite oxide interface.

In this work, we describe an interface, at which the B-site stacking order is based on the 1:1 B-site-ordered double-perovskite $Sr_2Fe_{1+x}Re_{1-x}O_6$ and the 1:2 B-site-ordered triple-perovskite $Sr_3Fe_2ReO_9$. The atomic-scale structure, composition, and valence states of the resulting triple-/double-perovskite oxide interface are studied by using aberration-corrected scanning transmission electron microscopy (STEM), electron energy-loss spectroscopy (EELS), and nanodiffraction. In addition, given the rarity of the experimentally observed interface and the predicted modulation of magnetic coupling by B-site ordering periodicity, we employed electron magnetic circular dichroism (EMCD) as a high-spatial-resolution, element-specific magnetic spectroscopy technique. Since its experimental demonstration in the TEM,[23] EMCD has been developed through theory,[24–27] dynamical diffraction,[28,29] vortex,[30–33] channeling effect,[34] in-plane geometries,[35] and nanoscale[36,37] to atomic[38–41] magnetic measurements. All of the above were used to experimentally determine the B-site cation sequence, including the use of EMCD to probe the projected net Fe magnetic moment. We then perform first-principles calculations of a superlattice structure model of 1:1 B-site-ordered double-perovskite Sr_2FeReO_6 and the 1:2 B-site-ordered triple-perovskite $Sr_3Fe_2ReO_9$ based on the experimental results, to gain insight into interfacial magnetic coupling. By comparing different possible magnetic configurations, we find that exchange coupling between Fe and Re atoms at the interface between the triple perovskite and the double perovskite is prone to be FM, as a result of the difference in B-site periodicity and strong coupling between the Fe 3*d* and Re 5*d* orbitals, which differs from the AFM coupling between Fe and Re atoms exhibited by the bulk double- and triple-perovskite structures. Our results provide a strategy for tuning B-site cation order periodicity to construct perovskite oxide interfaces with emergent interfacial magnetic coupling, thus opening a promising avenue for the exploration of new concepts of materials for high-performance spintronics.

2. METHOD SECTION

2.1. Sample Preparation

Polycrystalline $Sr_2Fe_{1+x}Re_{1-x}O_6$ samples were synthesized from a nominal stoichiometric ratio of $SrCO_3$, Fe_2O_3, and ReO_3 powders using both a conventional solid-state method and spark plasma sintering with a Sumitomo Coal Mining SPS-1050. The $Sr_2[Fe]_{B_1}[Fe_xRe_{1-x}]_{B_2}O_6$ sample was produced from a nominal stoichiometric ratio of $SrCO_3$, Fe_2O_3, and ReO_3 powders, which were mixed thoroughly via ball milling and pressed into pellets. To address the volatility of Re, the $Sr_2[Fe]_{B_1}[Fe_{1/6}Re_{5/6}]_{B_2}O_6$ sample was synthesized with an excess of 15 mol% Re and therefore had no Re deficiency. The $Sr_3[Fe]_{B_1}[Fe]_{B_2}[Re]_{B_3}O_9/Sr_2[Fe]_{B_1}[Fe_{1/6}Re_{5/6}]_{B_2}O_6$ interface was found in certain crystalline particles in the $Sr_2[Fe]_{B_1}[Fe_xRe_{1-x}]_{B_2}O_6$ sample. TEM specimen preparation was performed using conventional methods of mechanical grinding, dimpling, polishing, and Ar ion milling using a Bal-Tec Res-101 system.

2.2. Atomic-Scale Structural and Chemical Characterization

Atomic-resolution high-angle annular dark-field (HAADF) scanning transmission electron microscopy (STEM) was performed using an FEI Titan 80–300 microscope equipped with a three-condenser-lens system, a monochromator unit, and a CEOS probe corrector. STEM imaging was carried out at an accelerating voltage of 300 kV using a probe current of 80 pA. Atomic-resolution HAADF STEM imaging was performed using a probe convergence semi-angle of 25 mrad. The HAADF detector inner and outer collection semi-angles were 64–200 mrad. Energy-dispersive X-ray spectroscopy (EDXS) elemental mapping was carried out at an accelerating voltage of 200 kV using an FEI Titan G2 80–200 CREWLEY equipped with FEI ChemiSTEM/Super-X EDXS detection technology comprising four Si drift detectors with an energy resolution of <136 eV at Mn **Kα**

Downloaded from pubs.acs.org/aamick/article-pdf/18/36/50054/6822221/am-2026-08939f.pdf by guest on 08 November 2026

https://doi.org/10.1021/acsami.6c08939
ACS Appl. Mater. Interfaces 2026, 18, 50054–50063

(10 kcps). The atomic occupancy of the A-site of Sr and B-site ordering of Fe/Re cations was investigated using EDXS elemental mapping of the Sr **Kα** signal at 14.133 keV, the Fe **Kα** signal at 6.405 keV, and the Re **Lα** signal at 8.652 keV in STEM mode. The datasets had a size of 218 × 479 × 2048 channels and were recorded for 1000 s, with total counts of approximately 1,423,026. The data were processed using Bruker Esprit software and homemade Python code. Statistical analysis of the cation compositions was obtained from elemental maps recorded over regions of several tens of nm in size for arbitrary grain orientations.

2.3. EELS Experimental Conditions

EELS and EMCD measurements were performed using FEI Cubed Themis 60–300 STEM operated at 300 kV X-FEG with a monochromator, a probe corrector, an image corrector, and equipped with a Gatan Quantum 965 ER spectrometer. The probe size used for the nanoscale EELS/EMCD experimental condition was approximately 2 nm under microprobe mode. The probe convergence semi-angle was approximately 0.84 mrad, and the EELS collection semi-angle was 1.91 mrad. The energy dispersion was 0.15 eV/channel, and the energy resolution, estimated from the full width at half maximum of the zero-loss peak, was approximately 0.9 eV. The Fe $L_{3,2}$ edges were acquired from the double- and triple-perovskite regions under two-beam diffraction conditions. EEL spectra were processed by zero-loss-peak deconvolution, pre-edge background subtraction, and normalization. No smoothing was applied to the EMCD difference spectra used for analysis.

2.4. First-Principles Calculations and Image Simulations

Magnetic and electronic structure calculations of the interface were performed using density functional theory (DFT) via the Vienna Ab initio Simulation Package.[42] In order to implement these calculations, the projector augmented wave (PAW)[43] method was used with a plane-wave basis, and the exchange–correlation interaction was treated using the Perdew–Burke–Ernzerhof (PBE) functional with the generalized gradient approximation (GGA).[44] A 3 × 1 × 6 k-point mesh was generated with a fine precision of 0.03 π/Ångstrom in the first irreducible Brillouin zone (BZ) using the Monkhorst–Pack method after performing convergence tests. The convergence criteria for total energy and maximum force were set to 10^{-5} eV and 0.01 eV/Å, respectively. The cut-off energy was set to 550 eV.

In order to ensure accuracy of the calculation, a quasi-Newton algorithm was utilized for initial geometric optimization. Spin polarization was considered when determining the magnetic structure. The DFT + U method was utilized to correct for self-interaction errors in systems involving transition-metal atoms.[45] Specifically, the on-site Coulomb repulsion U was set according to previous reports, with U_{eff} = 3.2 eV for Fe and U = 1 eV for Re.[46] Due to computational limitations, we were only able to consider 14 Å between adjacent interfaces in the four-state calculation. The interface models contained 120 and 240 atoms with lattice parameters of a = 5.61 Å, b = 26.89 Å, and c = 9.71 Å. All atom positions in the interface model were fully relaxed. The four-state calculations for the bulk triple-perovskite $Sr_3[Fe]_{B_1}[Fe]_{B_2}[Re]_{B_3}O_9$ with the $P\bar{3}m1$ space group and the double-perovskite $Sr_2[Fe]_{B_1}[Fe_xRe_{1-x}]_{B_2}O_6$ were performed in 2 × 2 supercells, each containing 60 atoms, using a 3 × 6 × 2 k-point mesh and a 12 × 7 × 4 k-point mesh for structure optimization and calculation of the DOS, respectively. Post-processing of the data was facilitated using the VASPKIT software package.[47]

Average formation energy of the triple-/double-perovskite oxide interface with different magnetic coupling settings was initially calculated according to eq 1:

$$E_{form} = \frac{E_{system} - E_{atoms}}{n} \quad (1)$$

In this expression, E_{form}, E_{system}, E_{atoms}, and n denote the formation energy, the ground state energies of the interface model and isolated atoms, and the number of atoms in the system, respectively.

The four-state method is a mapping analysis approach, in which one defines the spin dimer for each superexchange path of interest as a structural fragment that contains the two interacting spin sites. The electronic states of the spin dimer were calculated using first-principles calculations. The energy difference of the four states and the magnetic moment values collectively determine the exchange parameter J_{ij}, based on the Heisenberg spin Hamiltonian, eq 2:

$$H_{spin} = \sum_{i>j} J_{ij} S_i S_j \quad (2)$$

where J_{ij} is the exchange coupling parameter and S_i and S_j are the spin moment vectors at sites i and j, respectively.

Based on DFT-relaxed theoretical models, HAADF STEM image simulations were performed using the multi-slice method implemented in Dr. Probe software. Simulation parameters for the electron source and collection angles were consistent with the experimental conditions.[48]

3. RESULTS AND DISCUSSION

3.1. Experimental Determination of the Atomic Structure of the Triple-/Double-Perovskite Oxide Interface

A high-angle annular dark-field scanning transmission electron microscopy (HAADF STEM) image shows the interface between the 1:2 B-site-ordered triple-perovskite $Sr_3Fe_2ReO_9$ and the 1:1 B-site-ordered double-perovskite $Sr_2Fe_{1+x}Re_{1-x}O_6$ viewed along the $[1\bar{1}0]_{pc}$ zone axis (see Figure 1). Here, the x value in $Sr_2Fe_{1+x}Re_{1-x}O_6$ is used to measure the deviation from ideal 1:1 atomic occupation of Fe and Re in Sr_2FeReO_6. As a result of a local deficiency in Re caused by its volatility during the preparation process, the 1:2 B-site-ordered triple-perovskite $Sr_3Fe_2ReO_9$ phase could be synthesized in the parent phase of the 1:1 B-site-ordered double-perovskite $Sr_2Fe_{1+x}Re_{1-x}O_6$. The triple-perovskite phase is rare within a bulk, which can only be observed from the local sample region via high-resolution STEM imaging, rather than the macroscopic X-ray diffraction (XRD) technique, which was summarized in our previous study.[22] The crystal structure from XRD of the polycrystalline sample $Sr_2Fe_{1+x}Re_{1-x}O_6$ containing the triple-perovskite $Sr_3Fe_2ReO_9$ phase only shows the characteristic peaks (011) and (110) of the double-perovskite $Sr_2Fe_{1+x}Re_{1-x}O_6$ with the $I4/m$ space group.[22] The absence of distinct diffraction peaks corresponding to the triple-perovskite phase indicates its low volume fraction and limited long-range ordering. Consequently, the density of this double-/triple-perovskite oxide interface structure remains relatively low.

Atomic number (Z) contrast of atomic columns with different elemental compositions is visible in Figure 1a, with Fe (Z = 26) columns appearing weakest, Re (Z = 75) columns appearing strongest, and Sr (Z = 38) columns in between. The HAADF STEM image of the interface between the 1:2 B-site-ordered triple-perovskite $Sr_3Fe_2ReO_9$ and the 1:1 double-perovskite $Sr_2Fe_{1+x}Re_{1-x}O_6$ shows a different periodicity on each side of the interface. Nanodiffraction patterns recorded from the two phases are shown in Figure 1b,c. The different B-site ordering of the two phases leads to distinct symmetries that are reflected in their nanodiffraction patterns. In Figure 1b, fractional super-reflection spots such as $\frac{1}{3}\{\bar{1}1\bar{1}\}_{pc}$ and $\frac{2}{3}\{\bar{1}1\bar{1}\}_{pc}$ (marked using yellow triangles) indicate the presence of a triple periodicity along $\langle\bar{1}1\bar{1}\rangle_{pc}$ in 1:2 B-site-ordered

Downloaded from pubs.acs.org/aamick/article-pdf/18/36/50054/6822221/am-2026-08939f.pdf by guest on 08 November 2026

https://doi.org/10.1021/acsami.6c08939
ACS Appl. Mater. Interfaces 2026, 18, 50054−50063

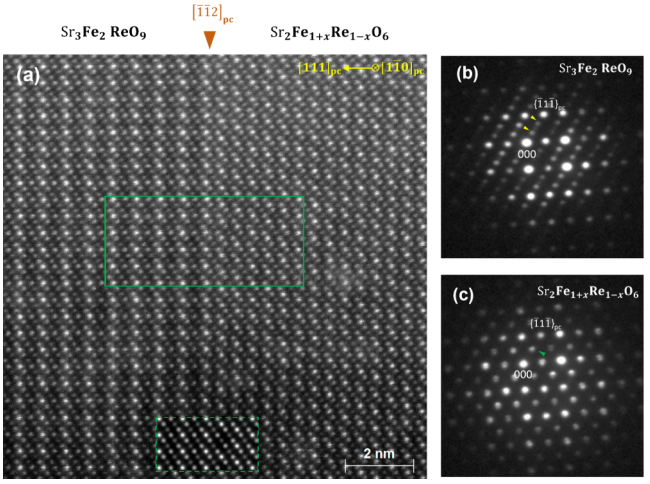


Figure 1. High-angle annular dark-field scanning transmission electron microscopy (HAADF STEM) image and nanodiffraction of the $Sr_3Fe_2ReO_9/Sr_2Fe_{1+x}Re_{1-x}O_6$ interface. (a) Green solid rectangle indicates the area used for elemental mapping. The inset in the green dashed rectangle shows a simulated HAADF STEM image of the $Sr_3Fe_2ReO_9/Sr_2Fe_{1+x}Re_{1-x}O_6$ interface based on the model shown in Figure 4a below. (b,c) Nanodiffraction patterns recorded from the 1:2 B-site-ordered $Sr_3Fe_2ReO_9$ phase and the 1:1 B-site-ordered $Sr_2Fe_{1+x}Re_{1-x}O_6$ phase, respectively. Fractional super-reflection spots (such as $\frac{1}{3}\{\bar{1}1\bar{1}\}_{pc}$, $\frac{2}{3}\{\bar{1}1\bar{1}\}_{pc}$) and half-integer super-reflection spots (such as $\frac{1}{2}\{\bar{1}1\bar{1}\}_{pc}$) are marked by yellow triangles in (b) and green triangles in (c), respectively.

$Sr_3Fe_2ReO_9$. In Figure 1c, half-integer super-reflection spots such as $\frac{1}{2}\{\bar{1}1\bar{1}\}_{pc}$ (marked using green triangles) are present in the double-perovskite $Sr_2Fe_{1+x}Re_{1-x}O_6$, indicating the presence of a double periodicity along $\boxtimes\bar{1}1\bar{1}_{pc}$.

The crystallographic character of the interface plane was further assessed using the pseudo-cubic framework. In both the 1:1 B-site-ordered double perovskite and the 1:2 B-site-ordered triple perovskite, the B-site ordering modulation occurs along the pseudo-cubic $[111]_{pc}$ direction, corresponding to alternating B-cation planes normal to $[111]_{pc}$. In the HAADF-STEM projection, the observed interface trace, marked by orange triangles in Figures 1 and 2, separates regions with distinct 1:1 and 1:2 B-site periodicities while preserving coherent corner-sharing perovskite connectivity across shared Fe/Re–O octahedral networks. Therefore, the experimentally observed interface is assigned to a pseudo-cubic $(111)_{pc}$-type plane, across which the B-site stacking sequence changes from $-[Fe–Fe–Re]_n-$ on the triple-perovskite side to $-[Fe–Re]_n-$ or Fe-rich $-[Fe–Fe_{1/6}Re_{5/6}]_n-$ ordering on the double-perovskite side. This assignment is consistent with the nanodiffraction evidence for $1/3[111]^*$ and $1/2[111]^*$ ordering vectors and with the DFT interface model used for the magnetic coupling calculations.

The atomic-resolution elemental maps shown in Figure 2 reveal atomic columns of Sr, Fe, and Re in green, red, and blue, respectively. The two phases are connected by shared Re and Fe atoms. The arrangement of Fe and Re atoms in the triple-perovskite $Sr_3Fe_2ReO_9$ phase is highly ordered, without visible anti-site occupation. In contrast, in the double-perovskite $Sr_2Fe_{1+x}Re_{1-x}O_6$ phase, Fe atoms occupy B_1 sites and additional Fe atoms appear randomly on the original B_2 positions of Re atoms. Furthermore, as shown in Figure S1, the quantitative statistical analysis of energy-dispersive X-ray spectroscopy (EDXS) spectra recorded from a relatively large area under the off-axis conditions suggests that the Fe/Re ratios are 2.02 ± 0.03 (~2:1) and 1.39 ± 0.03 (~7:5) for the triple-perovskite $Sr_3[Fe]_{B_1}[Fe]_{B_2}[Re]_{B_3}O_9$ and double-perovskite $Sr_2[Fe]_{B_1}[Fe_{1/6}Re_{5/6}]_{B_2}O_6$, respectively. The 1:2 B-site-ordered $-[Fe–Fe–Re]_n-$ in the triple-perovskite $Sr_3[Fe]_{B_1}[Fe]_{B_2}[Re]_{B_3}O_9$ and the 1:1 B-site-ordered $-[Fe–Fe_{1/6}Re_{5/6}]_n-$ in the double-perovskite $Sr_2[Fe]_{B_1}[Fe_{1/6}Re_{5/6}]_{B_2}O_6$ are clearly distinguished and consistent with the Z contrast of the images shown in Figure 1a.

To precisely determine the position of the interface, a unit-cell-by-unit-cell analysis of the Fe:Re ratio was conducted across the triple-/double-perovskite oxide interfaces, as shown in Figure 2e. The elemental mapping region contains a 218 × 479-pixel spectrum image with 2048 energy channels; the real-space scan area is approximately 5.81 nm × 2.64 nm. Figure 2f shows Fe:Re ratios close to 2 on the triple-perovskite side. Across the interface, the local projected ratio decreases to approximately 1.4 and then increases gradually to approximately 1.7 further into the double-perovskite region. The ratios represent the average statistical result obtained from the directly selected region of specific phases. The definition of the interface is determined by the location with a significant change in the Fe:Re ratio indicated by the orange triangles in Figure 2e,f. The deviation is caused by local variations in Re content resulting from the volatility of Re during sample growth. It is also noted that there is a discrepancy in the Fe:Re ratio obtained from EDXS mapping through Bruker Esprit software. A local Fe:Re ratio of approximately 1.7 is observed under zone-axis conditions, whereas a broader area yields a ratio close to 1.4 under off-axis conditions. This variation may be attributed to the nonuniform distribution of Fe and Re atoms and the channeling effect[49,50] inherent to EDXS measurements collected along the zone axis. For the quantitative numerical processing methods, please refer to the Supporting Information.

3.2. Phase-Resolved EMCD Measurements of the Projected Fe Magnetic Response

The valence states of Fe atoms in the two phases were assessed from a combined comparison of the Fe L_3-edge energy position, the $L_{3,2}$ white-line fine structure, and the L_3/L_2 white-line intensity ratio with reference Fe-oxide spectra previously reported Fe^{3+} electron energy-loss (EEL) spectra.[51] The spectra acquired from the double-perovskite $Sr_2[Fe]_{B_1}[Fe_{1/6}Re_{5/6}]_{B_2}O_6$ and the triple-perovskite $Sr_3[Fe]_{B_1}[Fe]_{B_2}[Re]_{B_3}O_9$ regions exhibit closely similar L_3-edge positions and white-line shapes, supporting the assignment of predominantly trivalent Fe in both regions within the energy resolution of the present measurements.[17] The change in valence most likely occurs for Re, which is understandable due to the larger width of the 5*d* band of Re than the 3*d* band of Fe. As a result of the stable chemical valences of Sr^{2+} and O^{2-}, the unchanged valence of Fe^{3+}, and conservation of charge, the valence states of $Sr_2[Fe]_{B_1}[Fe_{1/6}Re_{5/6}]_{B_2}O_6$ and $Sr_3[Fe]_{B_1}[Fe]_{B_2}[Re]_{B_3}O_9$ can be inferred to be $Sr_2[Fe^{3+}]_{B_1}[Fe_{1/6}^{3+}Re_{5/6}^{5.4+}]_{B_2}O_6$ and $Sr_3[Fe^{3+}]_{B_1}[Fe^{3+}]_{B_2}[Re^{6+}]_{B_3}O_9$, respectively.

Figure 3b,c shows the normalized Fe electron magnetic circular dichroism (EMCD) spectra, as well as EEL spectra, recorded from a region of double-perovskite $Sr_2[Fe]_{B_1}[Fe_{1/6}Re_{5/6}]_{B_2}O_6$ and a region of triple-perovskite $Sr_3[Fe]_{B_1}[Fe]_{B_2}[Re]_{B_3}O_9$,

Downloaded from pubs.acs.org/aamick/article-pdf/18/36/50054/6822221/am-2026-08939f.pdf by guest on 08 November 2026

https://doi.org/10.1021/acsami.6c08939
ACS Appl. Mater. Interfaces 2026, 18, 50054–50063

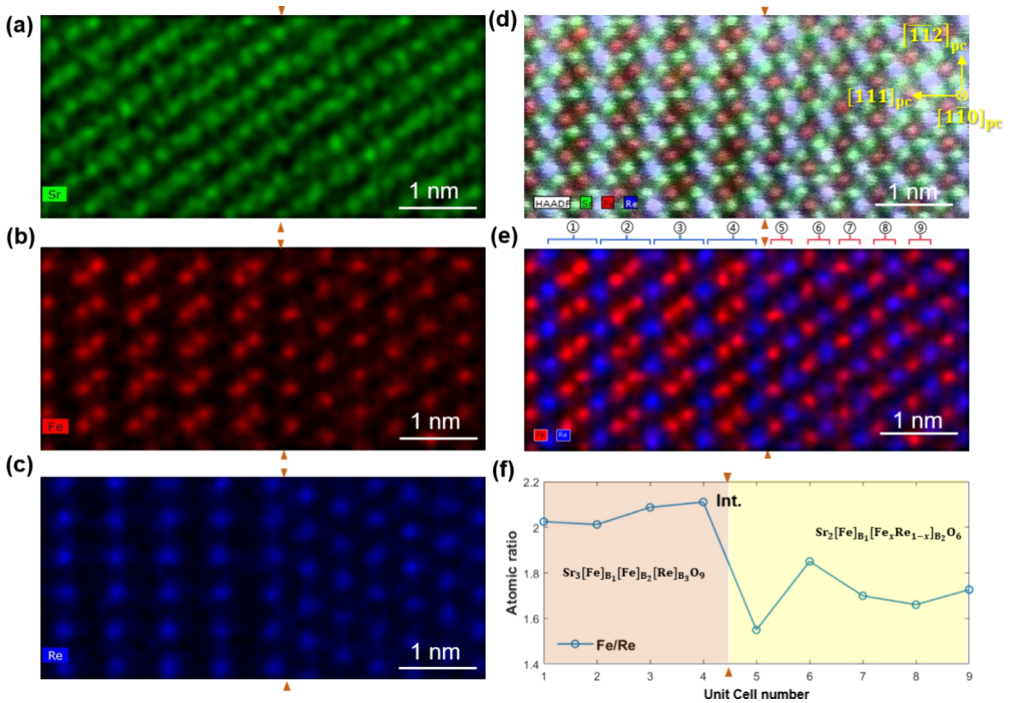


Figure 2. Atomic-resolution elemental mapping of the $Sr_3[Fe]_{B_1}[Fe]_{B_2}[Re]_{B_3}O_9/Sr_2[Fe]_{B_1}[Fe_{1/6}Re_{5/6}]_{B_2}O_6$ interface, showing (a) Sr in green, (b) Fe in red, (c) Re in blue, (d) elemental mixed Sr, Fe, and Re mapping as well as the HAADF STEM image, and (e) elemental mixed Fe and Re mapping. (f) Statistical Fe/Re ratios of the B-site transition metals on a unit cell by unit cell basis. On the triple-perovskite $Sr_3[Fe]_{B_1}[Fe]_{B_2}[Re]_{B_3}O_9$ side, the unit cell is –[Re–Fe–Fe]–, while on the double-perovskite $Sr_2[Fe]_{B_1}[Fe_xRe_{1-x}]_{B_2}O_6$ side, the nominal 1:1 unit cell is –[Fe–Re]–. For clarity, the unit number in (e) corresponds to that in (f), and the interface position is indicated by a pair of orange triangles.

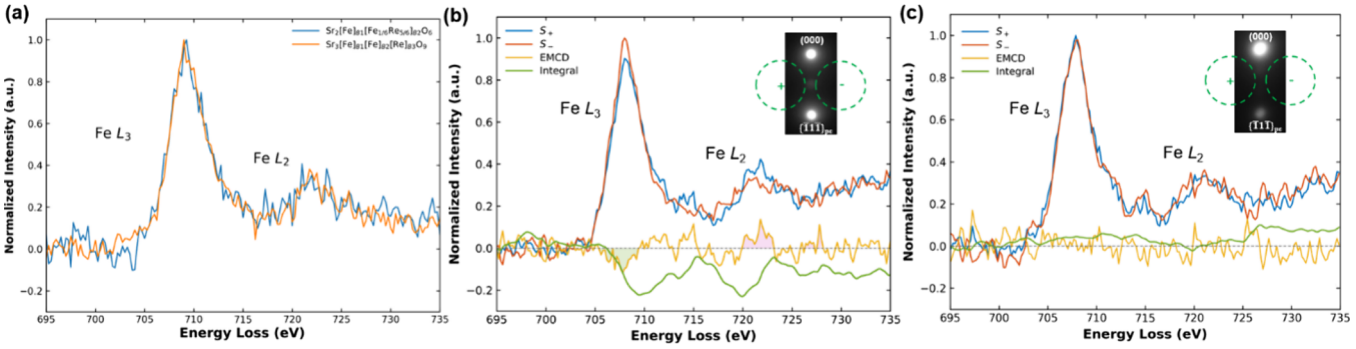


Figure 3. (a) Electron energy-loss (EEL) near-edge fine structures of the Fe $L_{3,2}$-edges acquired from the double- and triple-perovskite regions and used for Fe-valence assessment. Normalized EEL spectra acquired at the positive "S_+" (blue) and negative "S_-" (orange) positions from (b) double-perovskite $Sr_2[Fe]_{B_1}[Fe_{1/6}Re_{5/6}]_{B_2}O_6$ and (c) triple-perovskite $Sr_3[Fe]_{B_1}[Fe]_{B_2}[Re]_{B_3}O_9$ regions, respectively. The yellow lines show the electron magnetic circular dichroism (EMCD) spectra. The green lines show the cumulative integral of the residual-baseline-corrected difference spectrum. The insets were recorded under two-beam conditions, where $\{\bar{1}1\bar{1}\}_{pc}$ systematic reflections were excited with an electron probe.

respectively, at room temperature. The experimental EEL spectra marked by "S_+" (blue) and "S_-" (orange) were acquired at the positive (+) and negative (–) Thales positions, respectively, as indicated by green dotted circles in the insets, on the diffraction patterns under two-beam conditions with $\{1\bar{1}0\}_{pc}$ systematic reflections excited. The EMCD signal comes from the difference between the normalized "S_+" and "S_-" EEL spectra. The half-integer super-reflection spot of $\frac{1}{2}\{\bar{1}1\bar{1}\}_{pc}$ is present in the double-perovskite as shown in the inset of Figure 3b, while the very weak intensities of fractional super-reflection spots such as $\frac{1}{3}\{\bar{1}1\bar{1}\}_{pc}$ and $\frac{2}{3}\{\bar{1}1\bar{1}\}_{pc}$ as shown in the inset of Figure 3c indicate the presence of a triple periodicity along $\langle\bar{1}1\bar{1}\rangle_{pc}$ in 1:2 B-site-ordered $Sr_3Fe_2ReO_9$.

For EMCD acquisition, the specimen was tilted from the $[1\bar{1}0]_{pc}$ orientation to a two-beam condition by exciting the $\{\bar{1}1\bar{1}\}_{pc}$ systematic reflection. The required specimen tilt was approximately 7 degrees. The nanobeam convergence semi-angle was approximately 0.84 mrad related to the EELS collection semi-angle of 1.91 mrad. The yellow line in Figure 3b shows a significant Fe EMCD signal with opposite intensities at Fe L_3 and L_2 peaks in double-perovskite $Sr_2[Fe]_{B_1}[Fe_{1/6}Re_{5/6}]_{B_2}O_6$, indicating its ferrimagnetic coupling between Fe

https://doi.org/10.1021/acsami.6c08939
ACS Appl. Mater. Interfaces 2026, 18, 50054–50063

Downloaded from pubs.acs.org/aamick/article-pdf/18/36/50054/6822221/am-2026-08939f.pdf by guest on 08 November 2026

atoms at B_1 and B_2 sites. The green lines show the cumulative integral exhibiting a systematic excursion across the L_3 edge, followed by an oppositely directed contribution across the L_2 edge. This behavior is larger than the cumulative fluctuation obtained from the nonedge baseline regions and supports the presence of a statistically resolvable projected Fe dichroic response within the approximately 2 nm probed region. In comparison, the yellow line in Figure 3c reveals no comparable, statistically resolvable L_3/L_2 dichroic response in triple-perovskite $Sr_3[Fe]_{B_1}[Fe]_{B_2}[Re]_{B_3}O_9$, which is obtained under the same acquisition and processing conditions. This result establishes only that no projected net Fe magnetic response is resolved within the sensitivity and spatial averaging of the present experiment. It does not directly demonstrate antiferromagnetic coupling between Fe atoms at the B_1/B_2 sites, where distinguishing between compensated finite local moments, cancellation within the probed volume, an unfavorable projection of the magnetic moments, or a signal below the experimental detection limit remains challenging.

This observation is consistent with the theoretical prediction in our previous research.[22] Although our previous work demonstrated that the spatial resolution of the EMCD imaging can reach 4 Å with atomic plane resolution,[38] resolving the magnetic response plane by plane across the present $(111)_{pc}$-type interface would require a spatial resolution of approximately 2.2 Å under a suitable EMCD diffraction geometry, which is beyond the practical sensitivity of the present experiment. Extracting EMCD signals therefore provides complementary information on the projected Fe magnetic response across the double-/triple-perovskite oxide interface. Therefore, density functional theory (DFT) calculations can be employed to provide more insight into magnetic properties of the interfaces, which are constructed by the perovskite oxides with different B-site ordering periodicities.

3.3. First-Principles Comparison of Competing Interfacial Magnetic Configurations

The experimentally determined B-site stacking sequence is used as the structural constraint for the DFT + U interface model. However, the local spin directions at the interface are not assigned from the EMCD experiment. Instead, ferromagnetically and antiferromagnetically coupled interfacial configurations are introduced separately as alternative theoretical starting configurations, relaxed, and compared through their calculated energies and exchange parameters. The experimentally resolved cation arrangement is therefore used as the structural basis for the first-principles calculations, while the alternative magnetic configurations are introduced as theoretical hypotheses rather than as experimentally assigned spin states.

In order to investigate interfacial magnetic coupling modulated by the periodicity of B-site stacking ordering, we constructed a superlattice model of 1:2 B-site-ordered triple-perovskite $Sr_3[Fe]_{B_1}[Fe]_{B_2}[Re]_{B_3}O_9$ with space group $P\bar{3}m1$[22] and 1:1 B-site-ordered double-perovskite $Sr_2[Fe]_{B_1}[Re]_{B_2}O_6$ with space group $I4/m$,[46] containing triple-/double-perovskite oxide interfaces with 120 atoms in total with the available computational resources (cf. Figure 4a). The B-site ordering at the triple-/double-perovskite oxide interface in this model is consistent with the experimental observations of the atomic structure shown in Figures 1 and 2. Here, we select $Sr_3[Fe]_{B_1}[Fe]_{B_2}[Re]_{B_3}O_9$ with space group $P\bar{3}m1$, which is energetically more stable than that with space group $P\bar{3}c1$ as demonstrated in our previous study.[22] To focus on the effect of the B-site-ordered periodicity, an ideal Fe:Re ratio of 1:1 was adopted in double-perovskite $Sr_2[Fe]_{B_1}[Re]_{B_2}O_6$. It is worth noting that the experimental Fe:Re ratio in double-perovskite oxides is larger than 1:1, so the effect of excess Fe atoms occupying the B_2 sites on the interfacial magnetic coupling is discussed in detail in the Supporting Information.

The ground states of magnetic structures of the triple-perovskite $Sr_3[Fe]_{B_1}[Fe]_{B_2}[Re]_{B_3}O_9$ phase[22] and the double-perovskite $Sr_2[Fe]_{B_1}[Re]_{B_2}O_6$ phase[52] as shown in Figure 4b,c, respectively, reveal G-type AFM coupling of nearest-neighbor Fe and Re cations or Fe and Fe cations between adjacent $\{111\}_{pc}$ planes due to Fe–O–Re and Fe–O–Fe superexchange interactions. To evaluate the energetically favorable magnetic structure of the $Sr_3[Fe]_{B_1}[Fe]_{B_2}[Re]_{B_3}O_9/Sr_2[Fe]_{B_1}[Re]_{B_2}O_6$ interfaces, the formation energies of four magnetic structures including nonmagnetic structure (cf. Figure S2a), FM structure (cf. Figure S2b), AFM structures with antiferromagnetically coupled interfaces (cf. Figure S2c), and ferromagnetically coupled interfaces (cf. Figure S2d) were calculated. As summarized in Table S1, the calculations demonstrate that the AFM structure with the ferromagnetically coupled interface has the lowest formation energy, which is 5 meV/atom lower than that of the AFM structure with the antiferromagnetically coupled interface. The Re and Fe atomic layers at the very interface energetically favor FM coupling rather than AFM coupling in the bulk phases.

To further investigate the effect of the interaction between Fe 3d and Re 5d orbitals on interfacial magnetic coupling, we calculated the projected density of states (DOS) of adjacent Fe and Re layers at the very interface of $Sr_3[Fe]_{B_1}[Fe]_{B_2}[Re]_{B_3}O_9/Sr_2[Fe]_{B_1}[Re]_{B_2}O_6$ marked by a blue shadow in Figure 4a with those of the adjacent Fe and Re layers in bulk triple-perovskite $Sr_3[Fe]_{B_1}[Fe]_{B_2}[Re]_{B_3}O_9$ (cf. Figure 4b) and double-perovskite $Sr_2[Fe]_{B_1}[Re]_{B_2}O_6$ (cf. Figure 4c). It is evident that the overlap between Fe 3d and Re 5d orbitals at the very interface of triple-/double-perovskite oxides with enhanced interplay at the orbital level is significantly larger than that observed in the bulk triple- and double-perovskite oxides, revealing the ferromagnetically coupled interface, which is consistent with the calculation results of formation energy in Table S1. In contrast, the local DOS of the adjacent Fe and Re layers in triple-perovskite $Sr_3[Fe]_{B_1}[Fe]_{B_2}[Re]_{B_3}O_9$ and double-perovskite $Sr_2[Fe]_{B_1}[Re]_{B_2}O_6$ show antiferromagnetic coupling between Fe and Re atoms in bulk phases.

Moreover, we applied the four-state method[37,53] to calculate the Fe–O–Re and Fe–O–Fe superexchange parameters (cf. Table 1) for the $Sr_3[Fe]_{B_1}[Fe]_{B_2}[Re]_{B_3}O_9/Sr_2[Fe]_{B_1}[Re]_{B_2}O_6$ interface, the triple-perovskite $Sr_3[Fe]_{B_1}[Fe]_{B_2}[Re]_{B_3}O_9$, and the double-perovskite $Sr_2[Fe]_{B_1}[Re]_{B_2}O_6$ (cf. Figure 4), further demonstrating ferromagnetic coupling between Fe and Re atoms at the very interface of $Sr_3[Fe]_{B_1}[Fe]_{B_2}[Re]_{B_3}O_9/Sr_2[Fe]_{B_1}[Re]_{B_2}O_6$. A negative value of the exchange parameters J indicates FM coupling, whereas a positive value indicates AFM coupling. The Fe–O–Re interface exhibits FM coupling for both pair ① and pair ②, with magnitudes of –0.0357 eV and –0.0228 eV, respectively, while all other positive J values of the pairs from ③ to ⑧ demonstrate AFM coupling at both sides of double- and triple-perovskite oxides in this interface model. These findings align with the results obtained from the calculations of formation energy and

Downloaded from pubs.acs.org/aamick/article-pdf/18/36/50054/6822221/am-2026-08939f.pdf by guest on 08 November 2026

https://doi.org/10.1021/acsami.6c08939
ACS Appl. Mater. Interfaces 2026, 18, 50054–50063

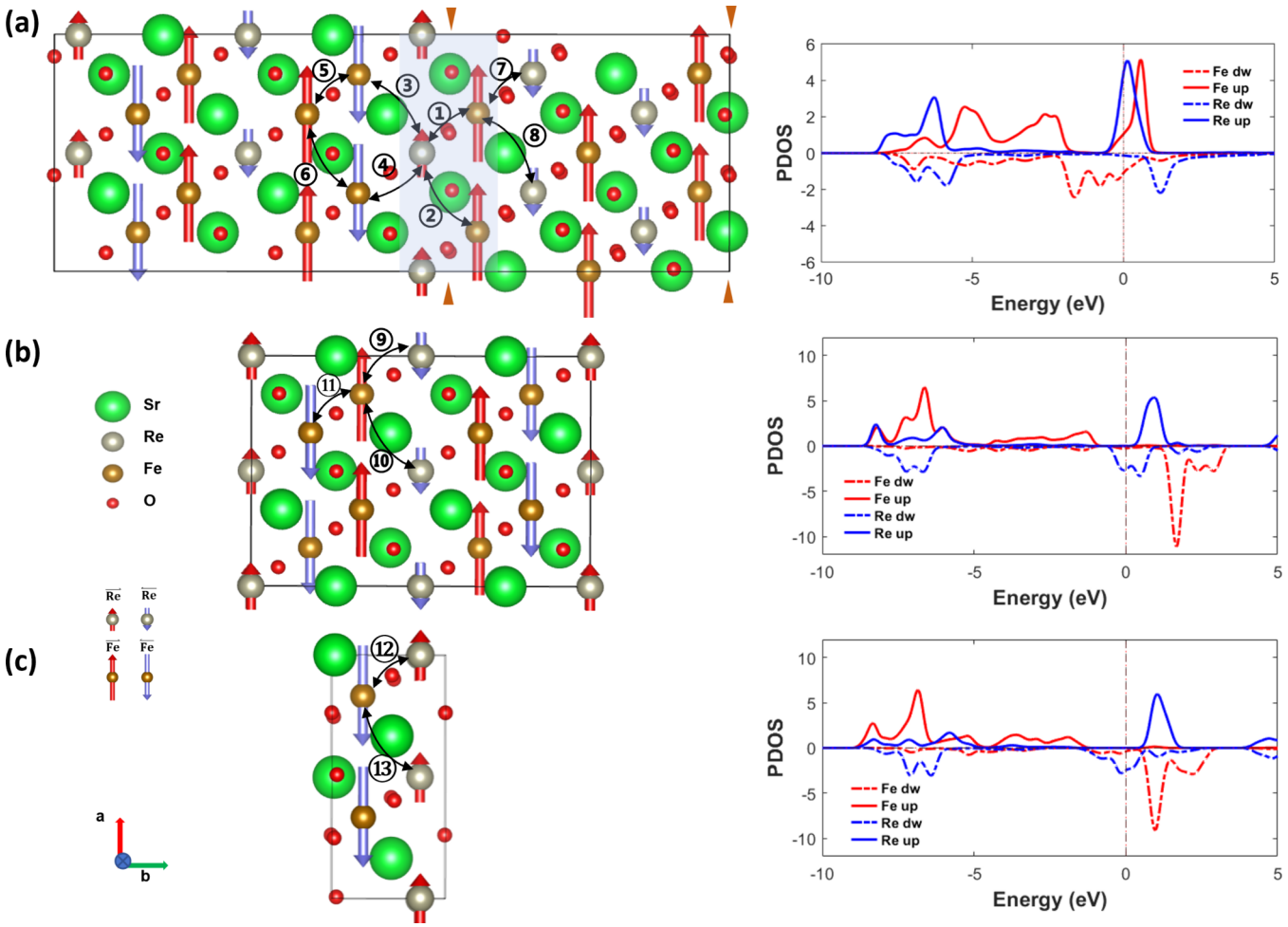


Figure 4. Atomic structure and magnetic coupling of (a) $Sr_3[Fe]_{B_1}[Fe]_{B_2}[Re]_{B_3}O_9/Sr_2[Fe]_{B_1}[Re]_{B_2}O_6$ interface model with the interface indicated by orange triangles, (b) $Sr_3[Fe]_{B_1}[Fe]_{B_2}[Re]_{B_3}O_9$ with the $P\bar{3}m1$ space group, and (c) $Sr_2[Fe]_{B_1}[Re]_{B_2}O_6$. The atomic structures in panels (a–c) show Sr in green, Re in silver, Fe in gold, and O in red. Spin-down and spin-up magnetic moments are represented by violet and red arrows, respectively. In the right figure in (a), the projected density of states (PDOS) of Fe and Re atoms at the very interface marked by a blue shadow reveals their ferromagnetic coupling, while in the right figures in (b) and (c), the PDOS of adjacent Fe and Re atoms show their antiferromagnetic coupling.

DOS. Previous research has indicated that in the double-perovskite $Sr_2[Fe]_{B_1}[Re]_{B_2}O_6$, which is a d^5-d^2 system with Fe in the 3+ state and Re in the 5+ state, local Hund exchange readily occurs, leading to d^4-d^3 charge fluctuations and the emergence of magnetism.[54] In the case of the triple-perovskite $Sr_3[Fe]_{B_1}[Fe]_{B_2}[Re]_{B_3}O_9$, our EELS measurements shown in Figure 3a indicate that the valence of Fe^{3+} remains the same, suggesting that there is an increase in the valence of Re from 5+ to 6+. This observation is understandable due to the lower localization of the 5*d* band of Re compared to the 3*d* band of Fe. The strong interaction between the electrons on Fe 3*d* and Re 5*d* orbitals, the magnetic coupling corresponding with LDOS as shown in Figure 4a, allows the electron hopping and exchange effect between adjacent Fe and Re atomic orbitals, which contributes to the interface FM coupling.

In addition, as previously noted, experimental observations reveal a Fe:Re ratio of 1.4:1 in the double-perovskite $Sr_2Fe_{1+x}Re_{1-x}O_6$, leading to a deviation from the ideal Fe:Re ratio of 1:1. We therefore constructed a 120-atom supercell model of the $Sr_3[Fe]_{B_1}[Fe]_{B_2}[Re]_{B_3}O_9/Sr_2[Fe]_{B_1}[Fe_{1/6}Re_{5/6}]_{B_2}O_6$ interface, with excess Fe occupancy at B_2 sites in the double-perovskite $Sr_2Fe_{1+x}Re_{1-x}O_6$ side (cf. Figure S7). The calculated formation energies, density of states, and exchange parameters show that the antiferromagnetic bulk regions with a ferromagnetically coupled interface remain energetically favorable in this Fe-substituted model (Tables S3 and S4). Separately, to assess finite-size effects in the ideal 1:1 interface model, we scaled up the $Sr_3[Fe]_{B_1}[Fe]_{B_2}[Re]_{B_3}O_9/Sr_2[Fe]_{B_1}[Re]_{B_2}O_6$ supercell from 120 to 240 atoms. The ferromagnetically coupled interface remained energetically preferred over the antiferromagnetically coupled configuration (Figure S10 and Table S2), indicating that this energy preference in the ideal interface model is not a finite-size artifact. By calculating the formation energy, DOS, and exchange coupling parameters with the same theoretical calculation methods as described in detail in the Supporting Information, it is also demonstrated that the AFM structures with ferromagnetically coupled interfaces are favorable in the $Sr_3[Fe]_{B_1}[Fe]_{B_2}[Re]_{B_3}O_9/Sr_2[Fe]_{B_1}[Fe_{1/6}Re_{5/6}]_{B_2}O_6$ interfaces. The periodicity of B-site stacking ordering, rather than excess Fe atoms, plays a dominant role in FM coupling at the double-/triple-perovskite oxide interfaces.

Downloaded from pubs.acs.org/aamick/article-pdf/18/36/50054/6822221/am-2026-08939f.pdf by guest on 08 November 2026

https://doi.org/10.1021/acsami.6c08939
ACS Appl. Mater. Interfaces 2026, 18, 50054–50063

Table 1. Exchange Parameters (J) (in eV) for the $Sr_3[Fe]_{B_1}[Fe]_{B_2}[Re]_{B_3}O_9/Sr_2[Fe]_{B_1}[Re]_{B_2}O_6$ Interface and Their Corresponding Ordered Structure $Sr_3[Fe]_{B_1}[Fe]_{B_2}[Re]_{B_3}O_9$ in the $P\bar{3}m1$ Space Group and $Sr_2[Fe]_{B_1}[Re]_{B_2}O_6$ with the $I4/m$ Space Group

structure	angle (deg)	pair	atoms	J (eV)	coupling type
$Sr_3[Fe]_{B_1}[Fe]_{B_2}[Re]_{B_3}O_9/Sr_2[Fe]_{B_1}[Re]_{B_2}O_6$ interface	166	1	Fe–Re	−0.0357	FM
	166	2	Fe–Re	−0.0228	FM
	179	3	Fe–Re	0.0095	AFM
	179	4	Fe–Re	0.0091	AFM
	180	5	Fe–Fe	0.0114	AFM
	180	6	Fe–Fe	0.0129	AFM
	180	7	Fe–Re	0.0019	AFM
	170	8	Fe–Re	0.0067	AFM
$Sr_3[Fe]_{B_1}[Fe]_{B_2}[Re]_{B_3}O_9$	180	9	Fe–Re	0.0106	AFM
	180	10	Fe–Re	0.0049	AFM
	180	11	Fe–Fe	0.0408	AFM
$Sr_2[Fe]_{B_1}[Re]_{B_2}O_6$	180	12	Fe–Re	0.0437	AFM
	170	13	Fe–Re	0.0465	AFM

4. CONCLUSIONS

We identify atomic structure, valence state, and elemental distribution at the interfaces between ferrimagnetic double-perovskite $Sr_2Fe_{1+x}Re_{1-x}O_6$ and AFM triple-perovskite $Sr_3Fe_2ReO_9$ with different B-site ordering periodicities through atomic-scale HAADF STEM imaging, nanodiffraction, EDXS mapping, EELS, and nanobeam EMCD. The DFT calculations on the superlattice model of 1:1 B-site-ordered double-perovskite $Sr_2[Fe]_{B_1}[Re]_{B_2}O_6$ and 1:2 B-site-ordered triple-perovskite $Sr_3[Fe]_{B_1}[Fe]_{B_2}[Re]_{B_3}O_9$ with the same B-site ordering modulation observed experimentally reveal emergent FM coupling between Fe and Re atoms at the interfaces due to the enhanced hybridization between Fe 3*d* and Re 5*d* orbitals in the density of states analysis. By comparison, the calculations indicate that adjacent Fe and Re atoms in both parent phases favor antiferromagnetic coupling. The experimentally resolved ordering discontinuity, together with the calculated preference for ferromagnetic interfacial coupling, suggests that B-site ordering periodicity may provide a route to tune interfacial magnetic interactions. This concept may be relevant to the design of epitaxial thin films with engineered interface magnetism, although direct experimental verification of the interfacial spin configuration remains necessary.

■ ASSOCIATED CONTENT

Supporting Information

The Supporting Information is available free of charge at https://pubs.acs.org/doi/10.1021/acsami.6c08939.

Quantitative STEM EDXS analysis of the double- and triple-perovskite regions (Figure S1); magnetic-structure models and density-of-states calculations (Figures S2 and S3); atomic-resolution EDXS data processing, unit-cell Fe:Re quantification, and ROI sensitivity analysis (Figures S4 and S5 and Table S6); effects of Fe substitution on interfacial structure, electronic states, and magnetic coupling, including projected density-of-states and 240-atom supercell calculations (Figures S6–S10); formation energies, exchange parameters, and Coulomb-repulsion tests (Tables S1–S5) in Supplementary figures and tables (PDF)

■ AUTHOR INFORMATION

Corresponding Authors

Ping-Luen Baron Ho – *Department of Materials and London Centre for Nanotechnology, Imperial College London, London SW7 2AZ, U.K.; Wolfson Catalysis Centre, Inorganic Chemistry Laboratory, Department of Chemistry, University of Oxford, Oxford OX1 3QR, U.K.;* orcid.org/0000-0002-3911-7973; Email: p.ho@imperial.ac.uk

Xiaoyan Zhong – *TRACE EM Unit, Department of Materials Science and Engineering, and Hong Kong Institute for Clean Energy (HKICE), City University of Hong Kong, Kowloon, Hong Kong, China; City University of Hong Kong Matter Science Research Institute (Futian, Shenzhen), Shenzhen 518048, China; Nanomanufacturing Laboratory (NML), City University of Hong Kong Shenzhen Research Institute, Shenzhen 518057, China;* orcid.org/0000-0001-8990-2198; Email: xzhong25@cityu.edu.hk

Authors

Jie Ren – *TRACE EM Unit, Department of Materials Science and Engineering, and Hong Kong Institute for Clean Energy (HKICE), City University of Hong Kong, Kowloon, Hong Kong, China; City University of Hong Kong Matter Science Research Institute (Futian, Shenzhen), Shenzhen 518048, China; Nanomanufacturing Laboratory (NML), City University of Hong Kong Shenzhen Research Institute, Shenzhen 518057, China;* orcid.org/0000-0001-5226-3783

Lei Jin – *Ernst Ruska-Centre for Microscopy and Spectroscopy with Electrons, Forschungszentrum Jülich GmbH, 52425 Jülich, Germany;* orcid.org/0000-0001-6924-2364

Si-Young Choi – *Department of Materials Science and Engineering, Pohang University of Science and Technology (POSTECH), Pohang 37673, South Korea; Center for Van der Waals Quantum Solids, Institute for Basic Science (IBS), Pohang 37673, South Korea; Department of Semiconductor Engineering, Pohang University of Science and Technology (POSTECH), Pohang 37673, South Korea;* orcid.org/0000-0003-1648-142X

Rafal E. Dunin-Borkowski – *Ernst Ruska-Centre for Microscopy and Spectroscopy with Electrons, Forschungszentrum Jülich GmbH, 52425 Jülich, Germany*

Joachim Mayer – *Ernst Ruska-Centre for Microscopy and Spectroscopy with Electrons, Forschungszentrum Jülich GmbH, 52425 Jülich, Germany; Central Facility for Electron Microscopy, RWTH Aachen University, 52074 Aachen, Germany;* orcid.org/0000-0003-3292-5342

Sandrine E. M. Heutz – *Department of Materials and London Centre for Nanotechnology, Imperial College London, London SW7 2AZ, U.K.;* orcid.org/0000-0003-3601-9320

Michele Shelly Conroy – *Department of Materials and London Centre for Nanotechnology, Imperial College London, London SW7 2AZ, U.K.*

Shik Chi Edman Tsang – *Wolfson Catalysis Centre, Inorganic Chemistry Laboratory, Department of Chemistry, University of*

Downloaded from pubs.acs.org/aamick/article-pdf/18/36/50054/6822221/am-2026-08939f.pdf by guest on 08 November 2026

https://doi.org/10.1021/acsami.6c08939
ACS Appl. Mater. Interfaces 2026, 18, 50054−50063

Oxford, Oxford OX1 3QR, U.K.; orcid.org/0000-0002-8796-3146

Complete contact information is available at: https://pubs.acs.org/doi/10.1021/acsami.6c08939

Author Contributions

‡J.R. and P.-L.B.H. contributed equally to this work. The manuscript was written through contributions of all authors. All authors have given approval to the final version of the manuscript.

Funding

This work was supported financially by the National Natural Science Foundation of China (52171014), the Guangdong Provincial Department of Science and Technology (2024A1515012303), the Sino-German Mobility Programme of the Sino-German Center for Research Promotion (M-0265), the City University of Hong Kong (Project nos. 7020207, 7030048, 9610484, 9680291, 9678288, 9610607), and the City University of Hong Kong Shenzhen Research Institute. The work described in this paper was supported substantially by a grant from the EU-HK Research and Innovation Cooperation Co-funding Mechanism sponsored by the Research Grants Council of the Hong Kong Special Administrative Region, China (Project No. E-CityU101/20) and the Research Grants Council of the Hong Kong Special Administrative Region, China (Project No. C1013-23E, C1018-22E, CityU 11309822). This project has received funding from the European Research Council (ERC) under the European Union's Horizon 2020 research and innovation programme (Grant No. 856538, project "3D MAGiC"). P.-L.B.H. would like to acknowledge the funding from the Swire Charitable Trust and the EPSRC through Combining Advanced Materials for Interface Engineering (CAMIE, EP/X027074/1).

Notes

The authors declare no competing financial interest.

†S.C.E.T. passed away on 20 May 2025.

■ ACKNOWLEDGMENTS

This work made use of resources at the Ernst Ruska-Centre for Microscopy and Spectroscopy with Electrons at Forschungszentrum Jülich, the National Centre for Electron Microscopy in Beijing, and the TRACE EM center at City University of Hong Kong. The authors thank Zhihao Huang, Jing Zhu, Peter D. Nellist, Fu-Rong Chen, Jessica Wade, Kyung Song, and James P. Buban for valuable contributions to this work.

■ REFERENCES

(1) Ksoll, P.; Meyer, C.; Schüler, L.; Roddatis, V.; Moshnyaga, V. B-Site Cation Ordering in Films, Superlattices, and Layer-by-Layer-Grown Double Perovskites. *Crystals* **2021**, *11* (7), 734.

(2) Rondinelli, J. M.; May, S. J.; Freeland, J. W. Control of octahedral connectivity in perovskite oxide heterostructures: An emerging route to multifunctional materials discovery. *MRS Bull.* **2012**, *37* (3), 261–270.

(3) Ramesh, R.; Schlom, D. G. Creating emergent phenomena in oxide superlattices. *Nat. Rev. Mater.* **2019**, *4* (4), 257–268.

(4) Wang, H.; Tang, F.; Dhuvad, P. H.; Wu, X. Interface enhanced functionalities in oxide superlattices under mechanical and electric boundary conditions. *npj Comput. Mater.* **2020**, *6* (1), 52.

(5) Kaczmarek, A. C.; Rosenberg, E. R.; Song, Y.; Ye, K.; Winter, G. A.; Penn, A. N.; Gomez-Bombarelli, R.; Beach, G. S. D.; Ross, C. A. Atomic order of rare earth ions in a complex oxide: a path to magneto-taxial anisotropy. *Nat. Commun.* **2024**, *15* (1), 5083.

(6) Aruta, C.; Tebano, A. Thin Films and Superlattice Synthesis. In *Perovskites and Related Mixed Oxides*; Wiley, **2016**; pp 143–168.

(7) Takahashi, K. S.; Kawasaki, M.; Tokura, Y. Interface ferromagnetism in oxide superlattices of $CaMnO_3/CaRuO_3$. *Appl. Phys. Lett.* **2001**, *79* (9), 1324–1326.

(8) Li, W.; Zhu, B.; Zhu, R.; Wang, Q.; Lu, P.; Sun, Y.; Cafolla, C.; Qi, Z.; Chen, A.; Gao, P.; et al. Atomic-Scale Control of Electronic Structure and Ferromagnetic Insulating State in Perovskite Oxide Superlattices by Long-Range Tuning of BO_6 Octahedra. *Adv. Funct. Mater.* **2020**, *30* (40), 2001984.

(9) Zhou, Y.; Kouser, S.; Borisevich, A. Y.; Pantelides, S. T.; May, S. J. Evidence for Interfacial Octahedral Coupling as a Route to Enhance Magnetoresistance in Perovskite Oxide Superlattices. *Adv. Mater. Interfaces* **2020**, *7* (9), 1901576 .

(10) Xu, H.; Chen, F.; Chen, B.; Jin, F.; Ma, C.; Xu, L.; Guo, Z.; Qu, L.; Lan, D.; Wu, W. Synthetic Antiferromagnets with Steplike Hysteresis Loops and High-T_C Based on All-Perovskite $La_{0.7}Sr_{0.3}MnO_3$ Superlattices. *Phys. Rev. Appl.* **2018**, *10* (2), 024035.

(11) Ueda, K.; Tabata, H.; Kawai, T. Ferromagnetism in $LaFeO_3$-$LaCrO_3$ Superlattices. *Science* **1998**, *280* (5366), 1064–1066.

(12) Li, M.-R.; Retuerto, M.; Deng, Z.; Stephens, P. W.; Croft, M.; Huang, Q.; Wu, H.; Deng, X.; Kotliar, G.; Sánchez-Benítez, J.; et al. Giant Magnetoresistance in the Half-Metallic Double-Perovskite Ferrimagnet Mn_2FeReO_6. *Angew. Chem., Int. Ed.* **2015**, *54* (41), 12069–12073.

(13) Arévalo-López, A. M.; McNally, G. M.; Attfield, J. P. Large Magnetization and Frustration Switching of Magnetoresistance in the Double-Perovskite Ferrimagnet Mn_2FeReO_6. *Angew. Chem., Int. Ed.* **2015**, *54* (41), 12074–12077.

(14) Li, M.-R.; McCabe, E. E.; Stephens, P. W.; Croft, M.; Collins, L.; Kalinin, S. V.; Deng, Z.; Retuerto, M.; Sen Gupta, A.; Padmanabhan, H.; et al. Magnetostriction-polarization coupling in multiferroic Mn_2MnWO_6. *Nat. Commun.* **2017**, *8* (1), 2037.

(15) Nakamura, T.; Choy, J.-H. Determination of ionic valency pairs via lattice constants in ordered perovskites $(ALa)(Mn^{2+}Mo^{5+})O_6$ (A = Ba, Sr, Ca) with applications to $(ALa)(Fe^{3+}Mo^{4+})O_6$, $Ba_2(Bi^{3+}Bi^{5+})O_6$ and $Ba_2(Bi^{3+}Sb^{5+})O_6$. *J. Solid State Chem.* **1977**, *20* (3), 233–244.

(16) Sohn, C.; Skoropata, E.; Choi, Y.; Gao, X.; Rastogi, A.; Huon, A.; McGuire, M. A.; Nuckols, L.; Zhang, Y.; Freeland, J. W.; et al. Room-Temperature Ferromagnetic Insulating State in Cation-Ordered Double-Perovskite $Sr_2Fe_{1+x}Re_{1-x}O_6$ Films. *Adv. Mater.* **2019**, *31* (4), 1805389.

(17) Ho, P.-L.; Yu, C.-P.; Zhang, Q.; Song, K.; Buban, J. P.; Choi, S.-Y.; Dunin-Borkowski, R. E.; Mayer, J.; Tai, N.-H.; Zhu, J.; et al. Effect of cation ratio and order on magnetic circular dichroism in the double perovskite $Sr_2Fe_{1+x}Re_{1-x}O_6$. *Ultramicroscopy* **2018**, *193*, 137–142.

(18) Lim, T.-W.; Kim, S.-D.; Sung, K.-D.; Rhyim, Y.-M.; Jeen, H.; Yun, J.; Kim, K.-H.; Song, K.-M.; Lee, S.; Chung, S.-Y.; et al. Insights into cationic ordering in Re-based double perovskite oxides. *Sci. Rep.* **2016**, *6* (1), 19746.

(19) Yang, L.; Fu, S.; Leng, K.; Tang, Q.; Wu, Z.; Yi, K.; Zhu, X. Crystal structure and magnetic properties of double perovskite Sr_2FeReO_6 ceramics synthesized by a combined molten-salt synthesis and solid-state reaction method. *Open Ceram.* **2022**, *9*, 100238.

(20) Abe, M.; Nakagawa, T.; Nomura, S. Magnetic and Mössbauer Studies of the Ordered Perovskites $Sr_2Fe_{1+x}Re_{1-x}O_6$. *J. Phys. Soc. Jpn.* **1973**, *35*, 1360–1365.

(21) Pannunzio Miner, E. V.; De Paoli, J. M.; Alonso, J. A.; García-Hernández, M.; Sánchez, R. D.; Carbonio, R. E. Ferrimagnetic order in the insulating $Sr_3Fe_2ReO_9$ double perovskite. *Phys. B* **2007**, *398* (2), 397–400.

Downloaded from pubs.acs.org/aamick/article-pdf/18/36/50054/6822221/am-2026-08939f.pdf by guest on 08 November 2026

(22) Ho, P.-L.; Huang, Z.; Jin, L.; Choi, S.-Y.; Dunin-Borkowski, R. E.; Mayer, J.; Tsang, S. C. E.; Zhong, X. Atomic-Scale Determination of Cation and Magnetic Order in the Triple Perovskite $Sr_3Fe_2ReO_9$. *Microsc. Microanal.* **2022**, *29* (1), 326–333.
(23) Schattschneider, P.; Rubino, S.; Hébert, C.; Rusz, J.; Kuneš, J.; Novák, P.; Carlino, E.; Fabrizioli, M.; Panaccione, G.; Rossi, G. Detection of magnetic circular dichroism using a transmission electron microscope. *Nature* **2006**, *441*, 486–488.
(24) Rusz, J.; Rubino, S.; Schattschneider, P. First-principles theory of chiral dichroism in electron microscopy applied to 3*d* ferromagnets. *Phys. Rev. B* **2007**, *75* (21), 214425.
(25) Barthel, J.; Mayer, J.; Rusz, J.; Ho, P. L.; Zhong, X. Y.; Lentzen, M.; Dunin-Borkowski, R. E.; Urban, K. W.; Brown, H. G.; Findlay, S. D.; et al. Understanding electron magnetic circular dichroism in a transition potential approach. *Phys. Rev. B* **2018**, *97* (14), 144103.
(26) Rusz, J.; Eriksson, O.; Novák, P.; Oppeneer, P. M. Sum rules for electron energy loss near edge spectra. *Phys. Rev. B* **2007**, *76* (6), 060408.
(27) Rusz, J.; Idrobo, J.-C.; Bhowmick, S. Achieving Atomic Resolution Magnetic Dichroism by Controlling the Phase Symmetry of an Electron Probe. *Phys. Rev. Lett.* **2014**, *113* (14), 145501.
(28) Lidbaum, H.; Rusz, J.; Rubino, S.; Liebig, A.; Hjörvarsson, B.; Oppeneer, P. M.; Eriksson, O.; Leifer, K. Reciprocal and real space maps for EMCD experiments. *Ultramicroscopy* **2010**, *110* (11), 1380–1389.
(29) Song, D.; Wang, Z.; Zhu, J. Effect of the asymmetry of dynamical electron diffraction on intensity of acquired EMCD signals. *Ultramicroscopy* **2015**, *148*, 42–51.
(30) Schachinger, T.; Löffler, S.; Steiger-Thirsfeld, A.; Stöger-Pollach, M.; Schneider, S.; Pohl, D.; Rellinghaus, B.; Schattschneider, P. EMCD with an electron vortex filter: Limitations and possibilities. *Ultramicroscopy* **2017**, *179*, 15–23.
(31) Schattschneider, P.; Löffler, S.; Stöger-Pollach, M.; Verbeeck, J. Is magnetic chiral dichroism feasible with electron vortices?. *Ultramicroscopy* **2014**, *136*, 81–85.
(32) Rusz, J.; Bhowmick, S.; Eriksson, M.; Karlsson, N. Scattering of electron vortex beams on a magnetic crystal: Towards atomic-resolution magnetic measurements. *Phys. Rev. B* **2014**, *89* (13), 134428.
(33) Zhong, X.; Lin, J.; Kao, S.; Liao, Z.; Zhu, J.; Huang, X.; Zhang, R.; Xin, H. L. Atomistic Defect Makes a Phase Plate for the Generation and High-Angular Splitting of Electron Vortex Beams. *ACS Nano* **2019**, *13* (4), 3964–3970.
(34) Wang, Z. Q.; Zhong, X. Y.; Yu, R.; Cheng, Z. Y.; Zhu, J. Quantitative experimental determination of site-specific magnetic structures by transmitted electrons. *Nat. Commun.* **2013**, *4* (1), 1395.
(35) Song, D.; Tavabi, A. H.; Li, Z.-A.; Kovács, A.; Rusz, J.; Huang, W.; Richter, G.; Dunin-Borkowski, R. E.; Zhu, J. An in-plane magnetic chiral dichroism approach for measurement of intrinsic magnetic signals using transmitted electrons. *Nat. Commun.* **2017**, *8* (1), 15348.
(36) Li, Z.; Lu, J.; Jin, L.; Rusz, J.; Kocevski, V.; Yanagihara, H.; Kita, E.; Mayer, J.; Dunin-Borkowski, R. E.; Xiang, H.; et al. Atomic Structure and Electron Magnetic Circular Dichroism of Individual Rock Salt Structure Antiphase Boundaries in Spinel Ferrites. *Adv. Funct. Mater.* **2021**, *31* (21), 2008306.
(37) Chen, X.; Higashikozono, S.; Ito, K.; Jin, L.; Ho, P.-L.; Yu, C.-P.; Tai, N.-H.; Mayer, J.; Dunin-Borkowski, R. E.; Suemasu, T.; et al. Nanoscale measurement of giant saturation magnetization in α″-$Fe_{16}N_2$ by electron energy-loss magnetic chiral dichroism. *Ultramicroscopy* **2019**, *203*, 37–43.
(38) Wang, Z.; Tavabi, A. H.; Jin, L.; Rusz, J.; Tyutyunnikov, D.; Jiang, H.; Moritomo, Y.; Mayer, J.; Dunin-Borkowski, R. E.; Yu, R.; et al. Atomic scale imaging of magnetic circular dichroism by achromatic electron microscopy. *Nat. Mater.* **2018**, *17* (3), 221–225.
(39) Ali, H.; Rusz, J.; Bürgler, D. E.; Vas, J. V.; Jin, L.; Adam, R.; Schneider, C. M.; Dunin-Borkowski, R. E. Visualizing subatomic orbital and spin moments using a scanning transmission electron microscope. *Nat. Mater.* **2025**, *24* (8), 1215–1220.
(40) Song, D.; Zheng, F.; Hao, L.; Jin, L.; Ke, Y.; Liu, Y.; Tian, M.; Ge, B.; Dunin-Borkowski, R. E.; Du, H. Magnetic circular dichroism imaging of atomic-scale antiferromagnetic order at a buried interface. *Nat. Nanotechnol.* **2026**, *21* (4), 523–529.
(41) Guzman, R.; Rusz, J.; Li, A.; Idrobo, J. C.; Zhou, W.; Gazquez, J. Detecting linear dichroism with atomic resolution. *Nat. Mater.* **2026**, .
(42) Kresse, G.; Furthmüller, J. Efficient iterative schemes for ab initio total-energy calculations using a plane-wave basis set. *Phys. Rev. B* **1996**, *54* (16), 11169–11186.
(43) Blöchl, P. E. Projector augmented-wave method. *Phys. Rev. B* **1994**, *50* (24), 17953–17979.
(44) Perdew, J. P.; Burke, K.; Ernzerhof, M. Generalized Gradient Approximation Made Simple. *Phys. Rev. Lett.* **1996**, *77* (18), 3865–3868.
(45) Hubbard, J. Electron correlations in narrow energy bands. *Proc. R. Soc. London, Ser. A* **1963**, *276*, 238–257.
(46) Jeng, H.-T.; Guo, G. Y. First-principles investigations of orbital magnetic moments and electronic structures of the double perovskites Sr_2FeMnO_6, Sr_2FeReO_6, and Sr_2CrWO_6. *Phys. Rev. B* **2003**, *67* (9), 094438.
(47) Wang, V.; Xu, N.; Liu, J.-C.; Tang, G.; Geng, W.-T. VASPKIT: A user-friendly interface facilitating high-throughput computing and analysis using VASP code. *Comput. Phys. Commun.* **2021**, *267*, 108033.
(48) Barthel, J. Dr. Probe: A software for high-resolution STEM image simulation. *Ultramicroscopy* **2018**, *193*, 1–11.
(49) MacArthur, K. E.; Brown, H. G.; Findlay, S. D.; Allen, L. J. Probing the effect of electron channelling on atomic resolution energy dispersive X-ray quantification. *Ultramicroscopy* **2017**, *182*, 264–275.
(50) Spurgeon, S. R.; Du, Y.; Chambers, S. A. Measurement Error in Atomic-Scale Scanning Transmission Electron Microscopy—Energy-Dispersive X-Ray Spectroscopy (STEM-EDS) Mapping of a Model Oxide Interface. *Microsc. Microanal.* **2017**, *23* (3), 513–517.
(51) Garvie, L. A. J.; Craven, A. J.; Brydson, R. Use of electron-energy loss near-edge fine structure in the study of minerals. *Am. Mineral.* **1994**, *79* (5-6), 411-425.
(52) Kobayashi, K. I.; Kimura, T.; Tomioka, Y.; Sawada, H.; Terakura, K.; Tokura, Y. Intergrain tunneling magnetoresistance in polycrystals of the ordered double perovskite Sr_2FeReO_6. *Phys. Rev. B* **1999**, *59* (17), 11159–11162.
(53) Xiang, H.; Lee, C.; Koo, H.-J.; Gong, X.; Whangbo, M.-H. Magnetic properties and energy-mapping analysis. *Dalton Trans.* **2013**, *42* (4), 823-853.
(54) Wang, H.; Zhu, S.; Ou, X.; Wu, H. Ferrimagnetism in the double perovskite Ca_2FeOsO_6: A density functional study. *Phys. Rev. B* **2014**, *90* (5), 054406.

Downloaded from pubs.acs.org/aamick/article-pdf/18/36/50054/6822221/am-2026-08939f.pdf by guest on 08 November 2026

https://doi.org/10.1021/acsami.6c08939
ACS Appl. Mater. Interfaces 2026, 18, 50054–50063